PERGAMON

International Journal of Heat and Mass Transfer 44 (2001) 2483–2492

International Journal of HEAT and MASS TRANSFER

www.elsevier.com/locate/ijhmt

A refined similarity solution for the multicomponent alloy solidification

Jae Dong Chung [a], Joon Sik Lee [a,*], Mansoo Choi [a], Hoseon Yoo [b]

[a] *School of Mechanical and Aerospace Engineering, Seoul National University, Seoul 151-742, South Korea*
[b] *Department of Mechanical Engineering, Soongsil University, Seoul 156-743, South Korea*

Received 24 May 2000; received in revised form 4 August 2000

Abstract

This paper deals with a refined similarity solution for the solidification of ternary or higher-order multicomponent alloys. The present approach not only retains the existing features of binary systems such as temperature–solute coupling, shrinkage-induced flow, solid–liquid property differences and finite back diffusion, but also is capable of handling a multicomponent alloy without restrictions on the partition coefficient and microsegregation parameter. A new exact solution to the energy equation including the convection term in the pure liquid region is successfully derived, which allows the present analysis to cover a high initial superheating. For an alloy of K-solute species, governing equations in the mushy region reduce to $(K+2)$ simultaneous ordinary differential equations via similarity transform, which are to be solved along with the closed-form temperature profiles in the solid and liquid regions. A linearized correction scheme adopted in the solution procedure facilitates to determine the solidus and liquidus position stably. Good agreements are found in comparison with the numerical predictions and available simplified similarity solutions for binary and ternary alloys.

1. Introduction

Analysis of alloy solidification processes has attracted considerable research attentions in heat and mass transfer area. Some of the recently developed numerical methods have shown a certain degree of success in qualitatively predicting the macroscopic features of alloy solidification [1,2]. Modeling efforts for incorporating the microscopic characteristics and/or interactions on different length scales into the numerical analysis have also been made [3,4]. From the viewpoint of alloy's composition, most of these studies have dealt with binary systems due mainly to a simple and well-defined nature of phase equilibrium relation. More recently, a number of notable attempts to predict the solidification behavior of multicomponent alloys have been reported [5–7]. They seem to be motivated by the fact that commercially used alloys are mostly composed of more than two constituents.

In developing a sophisticated numerical model for alloy solidification, one of the major problems is lack of appropriate benchmarks for quantitative assessment of the predicted results. Only a few sets of experimental data can be applied for model validation because uncertainties are associated with measurements, material properties and imposed conditions. In addition, the published analytical or semi-analytical solutions suffer from shortcomings associated with excessive simplifications in their derivation procedure or deviation from the actual phenomena, thereby being unable to capture the fundamental features of interest in the actual systems. The present study is intended to provide a more general test solution for the multicomponent alloy solidification.

A variety of analytical approaches to the alloy solidification problem in a one-dimensional domain have been proposed [8–10]. The latest two works of Voller [11] and Chung et al. [12] are worth to address among them, in that each of them tried to improve the previous studies in its own way. Voller [11] included the solute and temperature coupling, eutectic reaction,

* Corresponding author. Tel.: +82-2-880-7117; fax: +82-2-883-0179.
E-mail address: jslee@gong.snu.ac.kr (J.S. Lee).

0017-9310/01/$ - see front matter
PII: S0017-9310(00)00287-8

Nomenclature

c	specific heat
C	solute concentration
f	solid volume fraction
k	thermal conductivity
K	number of solute species
L	latent heat of fusion
P	coefficient
R	coefficient
t	time
T	temperature
ΔT	initial superheating, $T_0 - T_L$
x	coordinate

Greek symbols

α	thermal diffusivity
δ	position of the phase interface
η	similarity variable
κ	equilibrium partition coefficient
λ	transformed interface position, $\delta/(4\alpha_l t)^{1/2}$
ρ	density
ω	correction factor

Superscripts

$\bar{}$	phase-averaged quantity
$\hat{}$	ratio of the solid-to-liquid property
k	solute species
n	new value

Subscripts

0	initial condition
e	eutectic
i	microscopic solid–liquid interface
l	liquid
L	liquidus
m	mush
o	old value
s	solid
S	solidus
W	wall

microsegregation, shrinkage-induced flow, and macrosegregation in his model. This seems to be one of the most comprehensive test solutions for binary systems available in the literature, but still involves some limitations to be relaxed. First, the solution can actually be applicable to a binary system only, although it has been extended to handle a multicomponent alloy through his two companion papers [11,13]. It was assumed in the extension that both the microsegregation parameter and the partition coefficient are the same for all the solute species. However, this assumption leads the multicomponent system to an equivalent binary system because the transport of each solute is not independent. Second, convection in the bulk liquid was neglected, so that the solution can hardly cover the case of a high initial superheating. Third, all properties except the density were presumed to be constant for the sake of convenience of formulation. Noting that the effect of property variation has been a major concern in the previous studies [9,10], it needs to be retained for the completeness of analysis. Finally, the numerical algorithm for tracking the solidus and liquidus position, which plays the key role in analytical approaches, seems to be somewhat complicated to use.

Chung et al. [12] have presented a similarity solution for conduction-dominated binary alloy solidification. The effects of concentration-dependent solid fraction and variable properties in the mushy region were investigated for two representative binary systems. One of their major contributions is to develop a linearized correction scheme for tracking the phase interface positions. It appears to be efficient and ease to implement. Nevertheless, the study has drawback of dealing with binary alloys and excluding the shrinkage-induced flow.

The present study is aimed at refining the existing analytical approaches so as to handle a multicomponent system. It encompasses all the binary solidification features, but is free from the above-noted drawbacks. The analysis relies basically on the same similarity transformation as the previous studies. An exact solution to the full energy equation including the convection term in the bulk liquid is sought. Dependence of the mushy properties on the solid fraction is rigorously accounted for. The linearized correction scheme for locating the interfaces is extended to the present model. Finally, we compared the present results with available numerical and simplified analytical solutions of binary and ternary alloys.

2. Analysis

2.1. Modeling

The physical system considered in this work is a one-dimensional directional solidification, as depicted schematically in Fig. 1. At $t = 0$, the alloy, which was initially at a uniform concentration C_0^k for each solute k and at a superheated temperature T_0, begins to solidify in a semi-infinite domain from the isothermally cooled wall. The wall temperature T_W is lower than the eutectic temperature of the alloy, so that eutectic reaction takes place. As the solidification proceeds, three distinct

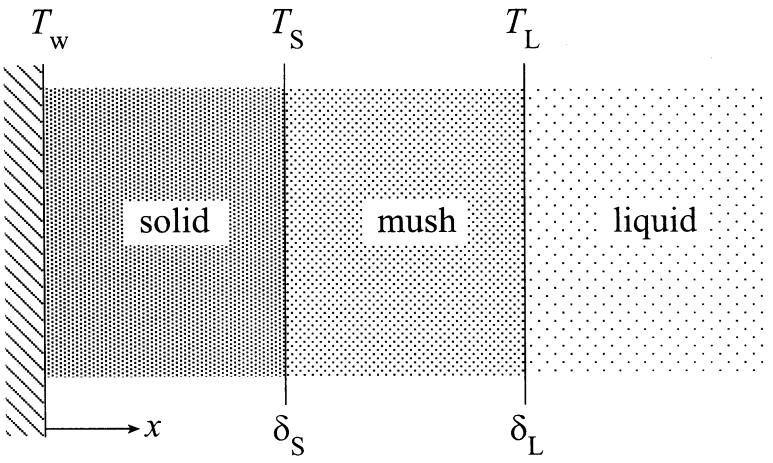

Fig. 1. Schematic of present multicomponent alloy solidification model.

regions, i.e., solid, mush, and liquid, bounded by the solidus and liquidus appear in the system. This model is basically identical with Voller's [11].

In order to render the problem analytically tractable, the following assumptions have been introduced:

1. The solid is fixed to the wall and is not deformed, i.e., the morphology of the mushy region is columnar dendritic or consolidated equiaxed.
2. Within a control volume of the mushy region, the temperature and interdendritic liquid concentration are uniform.
3. Thermodynamic equilibrium holds at the microscopic solid–liquid interface, i.e., $C_{si}^k = \kappa^k C_l^k$, where κ^k is the equilibrium partition coefficient for each solute k.
4. In a dilute system, assuming straight liquidus lines, the relation between the temperature and liquid concentrations of the solutes along the liquidus surface can be expressed as [5,13]

$$T = T_f + \sum_{k=1}^{K} m^k C_l^k, \tag{1}$$

where m^k is the liquidus slope of solute k and T_f is the fusion temperature of the pure solvent. This corresponds to the primary solidification path with isothermal eutectic troughs in Krane et al. [6].

5. The macroscopic solute diffusion is negligible. This implies that the solute transports both in the solid and pure liquid regions are absent.
6. Back diffusion in the dendritic solid is specified by Clyne and Kurz microsegregation model [14].
7. Flow is induced only by the solid–liquid density difference.
8. All properties are constant within individual phases, but may differ between the solid and liquid phases. Hence properties in the mushy region, where two phases coexist, are weighted by the solid fraction [9,10] as

$$\phi_m = f\phi_s + (1-f)\phi_l. \tag{2}$$

9. Inter-diffusion of each solute is neglected [6]. Then the species transport equation for each solute has the same form (see Eq. (6)).

The assumptions described above are the same as Voller's [11] except the assumptions (8) and (9). However, Voller's additional assumptions, i.e., a low superheating to neglect the convection effect in the liquid region and same microsegregation parameter and partition coefficient for each solute to deal with ternary alloys, have been relaxed.

Based on the foregoing assumptions, the governing equations are derived as follows [11,12]:

In the solid region ($0 < x < \delta_S$),

$$\frac{\partial T}{\partial t} = \alpha_s \frac{\partial^2 T}{\partial x^2}. \tag{3}$$

In the mushy region ($\delta_S < x < \delta_L$),

$$\frac{\partial u}{\partial x} = (1-\hat{\rho})\frac{\partial f}{\partial t}, \tag{4}$$

$$[f\hat{\rho}\hat{c} + (1-f)]\frac{\partial T}{\partial t} + u\frac{\partial T}{\partial x} + \left[\hat{\rho}T(\hat{c}-1) - \frac{L}{c_l}\hat{\rho}\right]\frac{\partial f}{\partial t} = \alpha_l \frac{\partial}{\partial x}\left[\{f\hat{k} + (1-f)\}\frac{\partial T}{\partial x}\right], \tag{5}$$

$$[(1-f) + \beta^k f\hat{\rho}\kappa^k]\frac{\partial C_l^k}{\partial t} + u\frac{\partial C_l^k}{\partial x} = (1-\kappa^k)C_l^k\hat{\rho}\frac{\partial f}{\partial t}, \tag{6}$$

where the hat symbol denotes the ratio of solid-to-liquid property.

In the liquid region ($\delta_L < x < \infty$),

$$\frac{\partial T}{\partial t} + u_l \frac{\partial T}{\partial x} = \alpha_l \frac{\partial^2 T}{\partial x^2}, \tag{7}$$

where the flow velocity in this region is defined as $u_l = u(\delta_L)$.

The initial condition is evident, and the boundary conditions are listed as follows:

$$T = T_W, \qquad \text{at} \quad x = 0, \tag{8}$$

$$u = (1 - f_S)(1 - \hat{\rho}) \frac{d\delta_S}{dt}, \qquad \text{at} \quad x = \delta_S, \tag{9}$$

$$T = T_S, \qquad \text{at} \quad x = \delta_S, \tag{10}$$

$$k_m \left(\frac{\partial T}{\partial x} \right)_m - k_s \left(\frac{\partial T}{\partial x} \right)_s = -\rho_s \frac{d\delta_S}{dt} (1 - f_S)[(c_l - c_s)T_S + L], \quad \text{at} \quad x = \delta_S, \tag{11}$$

$$T = T_L, \qquad \text{at} \quad x = \delta_L, \tag{12}$$

$$k_m \left(\frac{\partial T}{\partial x} \right)_m - k_l \left(\frac{\partial T}{\partial x} \right)_l = 0, \qquad \text{at} \quad x = \delta_L, \tag{13}$$

$$C_l^k = C_0^k, \qquad \text{at} \quad x = \delta_L, \tag{14}$$

$$T = T_0 \qquad \text{as} \quad x \to \infty, \tag{15}$$

where f_S is the solid fraction at the end of dendritic solidification, thereby $(1 - f_S)$ being the eutectic fraction.

The term β^k appearing in Eq. (6) represents the degree of back diffusion in the dendritic solid [14], by which the interaction between microsegregation and macrosegregation is incorporated. Settings of $\beta^k = 0$ and $\beta^k = 1$ respectively correspond to two limiting cases of solid state diffusion, i.e., the Scheil equation and the lever rule. Values in $0 < \beta^k < 1$ indicate finite back diffusion but have no physical meaning in Clyne and Kurz microsegregation model [14]. The solid fraction is continuous at the liquidus, whereas it jumps from f_S to 1 at the solidus on occurrence of eutectic reaction. As evident in Eq. (9), the velocity in the mushy region, u, traces the same trend.

Since the species transport equation is formulated separately for each solute, the present model can deal with a multicomponent alloy without restrictions on the partition coefficient and microsegregation parameter. It should be remarked here that the effects of both the partition coefficient and the liquid slope for individual solute species have shown to be significant in a numerical prediction [5]. The model equations also retain the convection term in the liquid energy conservation and property variation in the mushy region. These aspects differentiate the present study from the previous ones.

2.2. Similarity transformation

Analytical approaches are directed basically at reducing the governing partial differential equations to a set of algebraic and/or ordinary differential equations via variable transformations or approximations. Two commonly adopted methods, i.e. the heat balance integral and similarity transformation, have well been reviewed by Voller [11]. The present study prefers the similarity solution.

The well-known similarity variable

$$\eta = x/(4\alpha_l t)^{1/2}, \tag{16}$$

is introduced to reduce the model equations. In the solid region, the temperature profile is already available [11,12] as

$$\frac{T - T_W}{T_S - T_W} = \frac{\operatorname{erf}(\eta/\hat{\alpha}^{1/2})}{\operatorname{erf}(\lambda_S/\hat{\alpha}^{1/2})} \qquad \text{for} \quad 0 < \eta < \lambda_S, \tag{17}$$

where the transformed interface position is defined as $\lambda = \delta/(4\alpha_l t)^{1/2}$. In the liquid region, on the other hand, we are to derive an exact similarity solution. Since the velocity u_l is uniform throughout the liquid region, Eq. (7) is transformed into

$$\frac{d^2 T}{d\eta^2} + 2(\eta - U_l) \frac{dT}{d\eta} = 0, \tag{18}$$

where $U_l = u_l/(\alpha_l/t)^{1/2}$. Solving Eq. (18) subject to Eqs. (12) and (15) results in

$$\frac{T - T_0}{T_L - T_0} = \frac{\operatorname{erfc}(\eta - U_l)}{\operatorname{erfc}(\lambda_L - U_l)} \qquad \text{for} \quad \lambda_L < \eta < \infty. \tag{19}$$

Note here that the solidus and liquidus positions, λ_S and λ_L, and the velocity, U_l, are not known in Eqs. (17) and (19).

In the mushy region, the similarity transformation yields a set of ordinary differential equations, i.e.,

$$\frac{dU}{d\eta} + (1 - \hat{\rho})\eta \frac{df}{d\eta} = 0, \tag{20}$$

$$\frac{d}{d\eta}\left[\{f\hat{k} + (1 - f)\} \frac{dT}{d\eta} \right] = -2\{f\hat{\rho}\hat{c} + (1 - f)\}\eta \frac{dT}{d\eta} + 2U \frac{dT}{d\eta} - 2\left\{ \hat{\rho} T(\hat{c} - 1) - \frac{L}{c_l}\hat{\rho} \right\} \eta \frac{df}{d\eta}, \tag{21}$$

$$(1 - \kappa^k)\hat{\rho} C_l^k \eta \frac{df}{d\eta} + U \frac{dC_l^k}{d\eta} = \{(1 - f) + \beta^k \hat{\rho} f \kappa^k\} \eta \frac{dC_l^k}{d\eta}. \tag{22}$$

The boundary condition, Eq. (9), is also rewritten as

$$U = (1 - f_S)(1 - \hat{\rho})\lambda_S, \qquad \text{at} \quad \eta = \lambda_S. \tag{23}$$

For the closure of the analysis, the heat flux conditions at the solidus and liquidus, Eqs. (11) and (13), should be expressed in terms of the transformed variables. Taking advantage of Eqs. (17) and (19), the interfacial heat fluxes are rearranged as

$$\left(\frac{\mathrm{d}T}{\mathrm{d}\eta}\right)_{\lambda_S^+} = \frac{1}{f_S\hat{k}+(1-f_S)}\left[\frac{2}{(\pi\hat{\alpha})^{1/2}} \times \exp(-\lambda_S^2/\hat{\alpha})\frac{\hat{k}(T_S-T_W)}{\mathrm{erf}(\lambda_S/\hat{\alpha}^{1/2})} - 2\lambda_S\hat{\rho}(1-f_S)\left\{(1-\hat{c})T+\frac{L}{c_l}\right\}\right], \quad (24)$$

$$\left(\frac{\mathrm{d}T}{\mathrm{d}\eta}\right)_{\lambda_L^-} = \frac{2}{\pi^{1/2}}\frac{T_0-T_L}{\mathrm{erfc}(\lambda_L-U_l)}\exp\{-(\lambda_L-U_l)^2\}, \quad (25)$$

where λ_S^+ and λ_L^- denote the solidus and liquidus positions approaching from the mushy side, respectively.

2.3. Solution procedure

The transformed equations in the mushy region, Eqs. (20)–(22) along with the supplemental relation, Eq. (1), are to be solved to obtain $f(\eta)$, $T(\eta)$, $U(\eta)$ and $C_l^k(\eta)$. Also δ_S and δ_L should be determined as satisfying interfacial heat flux conditions, Eqs. (24) and (25). The inherent complexities stemming from the nonlinearities pose formidable barriers to straightforward analytical treatments in mushy region, so a numerical method is invoked. However, it should be noted that such a numerical approach is distinct from a direct numerical simulation of the system described by the original partial differential equations.

In order to compare the present results with Voller's [11,13] on the same condition used in his analysis, the mushy region is discretized into 4000 segments. At each iteration, velocity distribution is updated by integrating Eq. (20) from $\eta=\lambda_S$ to λ_L using Eq. (23). Eq. (21) subject to Eqs. (10) and (12) is solved to obtain the temperature distribution. One of the species equations, e.g., $k=1$ in Eq. (22), is assigned for renewing the solid fraction, while the others and Eq. (1) are used to determine the concentration fields of each solute. It is more convenient to integrate the species equation backward from $\eta=\lambda_L$ because of the well-defined boundary conditions, Eq. (14). Note that the relation between the temperature and liquid concentration does not need to be linear in the present analysis.

In order to determine the interface positions, a linearized correction scheme that proved to be efficient for a binary alloy [12], is adopted. The solidus and liquidus positions are corrected, respectively, as

$$\lambda_S^n = \lambda_S(1+\omega_S), \quad (26)$$

$$\lambda_L'^n = \lambda_L'(1+\omega_L), \quad (27)$$

where $\lambda_L' = \lambda_L - U_l$, and the superscript n denotes the new value during an iteration procedure. Substituting Eqs. (26) and (27) into Eqs. (24) and (25), respectively, expanding the results via the Taylor series, and truncating the higher-order terms, we have the following equations for the correction factors:

$$\omega_S[P_1P_4 + 2P_2\lambda_S^2/\hat{\alpha} + 2P_3\lambda_S\,\mathrm{erf}(\lambda_S/\hat{\alpha}^{1/2}) + 2P_1P_3\lambda_S] = -P_4\,\mathrm{erf}(\lambda_S/\hat{\alpha}^{1/2}) + P_2 - 2P_3\lambda_S\,\mathrm{erf}(\lambda_S/\hat{\alpha}^{1/2}), \quad (28)$$

$$\omega_L\exp(-\lambda_L'^2)\left[4R\lambda_L'^2 - \frac{2}{\pi^{1/2}}\lambda_L'\left(\frac{\mathrm{d}T}{\mathrm{d}\eta}\right)_{\lambda_L^-}\right] = 2R\exp(\lambda_L'^2) - \{1-\mathrm{erf}(\lambda_L')\}\left(\frac{\mathrm{d}T}{\mathrm{d}\eta}\right)_{\lambda_L^-}, \quad (29)$$

where the coefficients P_j $(j=1,\ldots,4)$ and R are defined as

$$P_1 = \frac{2\lambda_S}{(\pi\hat{\alpha})^{1/2}}\exp(-\lambda_S^2/\hat{\alpha}), \quad (30)$$

$$P_2 = \frac{2\hat{k}(T_S-T_W)}{(\pi\hat{\alpha})^{1/2}}\exp(-\lambda_L^2/\hat{\alpha}), \quad (31)$$

$$P_3 = \hat{\rho}(1-f_S)\left[(1-\hat{c})T_S+\frac{L}{c_l}\right], \quad (32)$$

$$P_4 = [f_S\hat{k}+(1-f_S)]\left(\frac{\mathrm{d}T}{\mathrm{d}\eta}\right)_{\lambda_S^+}, \quad (33)$$

$$R = (T_0-T_L)/\pi^{1/2}. \quad (34)$$

Since the performance of the interface tracking essentially affects the overall utility of the similarity solution, the development of an efficient routine is no less important than the modeling of physical phenomena. The present algorithm given below has shown stable and efficient convergence.

The final solution procedure is summarized as follows:

1. Guess the values of λ_S and λ_L.
2. Assume the profiles of $T(\eta)$, $f(\eta)$, $U(\eta)$, and $C_l^k(\eta)$ in $\lambda_S \leqslant \eta \leqslant \lambda_L$.
3. Solve Eqs. (20)–(22) along with Eq. (1), as described above. This sequential-iterative procedure continues until convergence.
4. On convergence at step (3), check whether the calculated temperature profile satisfies Eqs. (24) and (25) within a prescribed tolerance.
5. If not, calculate the correction factors from Eqs. (28) and (29), and update the interface positions using Eqs. (26) and (27). Repeat steps (3)–(5).

6. On satisfaction at step (4), terminate the procedure and calculate the quantities of interest.

In the actual calculations, it is recommended to under-relaxate ω values during correction stage, i.e., in applying to Eqs. (26) and (27), for ensuring stable convergence.

3. Results and discussion

3.1. Model validation

First of all, the present study is validated by comparing the results with available analytical and/or numerical solutions [11,13]. All the properties and conditions used here are identical with those of Swaminathan and Voller [13], and listed in Table 1. Note that a much larger than the observed difference between the solid and liquid densities is imposed to induce a strong interdendritic fluid flow. The starred values of c and k in parenthesis, which were cited from Chung et al. [12], are used only to examine the effect of property variation. Two sets of values in κ, m, and C_0 correspond to binary and ternary alloys, respectively.

Fig. 2 illustrates the mixture concentration profiles at the two extremes of back diffusion for a binary alloy. Independently of the degree of back diffusion, two sets of data agree excellently with each other. For a ternary alloy, Fig. 3 shows the mixture concentration profiles of solute A and B based on (i) zero back diffusion for both solutes, and (ii) complete back diffusion for solute A (lever rule) and zero back diffusion for solute B (Scheil equation). Complete agreement is found with the available numerical solution [13] for the case (i), but the deviation in the case (ii), especially in the profile of solute A is discernible. However, in view of favorable agreement for solute B and assumption (9) aforementioned, it can be deduced that the solid fraction profile is correctly obtained for the case (ii). Then the mixture concentration of solute A at the solidus interface can be evaluated using Eqs. (1) and (35), which implies that the numerical results [13] seem to under-predict the macrosegregation in the mushy region. Note that the above discussion is valid as far as the solid fraction coincide between the two studies. These comparisons give credence to the ascertainment that the present study has been carried out on proper modeling, formulation and solution procedure.

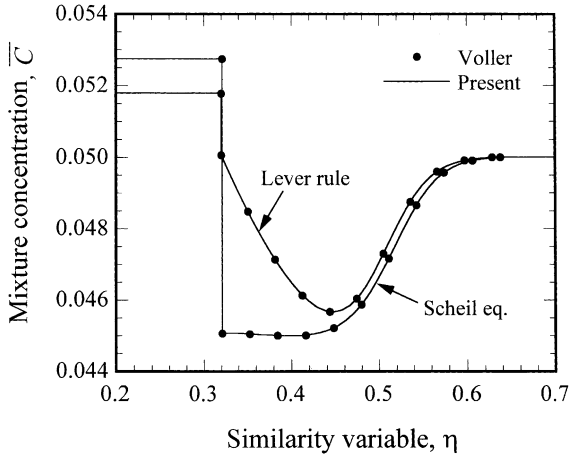

Fig. 2. Comparison of the average concentration profile between the present and previous solutions under the same conditions of constant properties and a small superheating.

Verification of the present model is also achieved by increasing the liquidus slope of one species, say A, and examining the asymptotic behavior towards a binary system. Fig. 4 shows the mixture concentrations of solute A and B for $\beta^k = 0$, according to the change of the liquidus slope of solute A, m^A. In this examination, the value of $m^A C_0^A$ has been kept constant to maintain invariant solidus and liquidus temperatures (see Eq. (1)). This implies that the mixture concentration of solute B is not disturbed and the present ternary model reduces to a

Table 1
Numerical data for sample binary and ternary alloys [11]

Property	Value		Unit
	Solid	Liquid	
c	1000	1000 (960*)	J kg^{-1} K^{-1}
k	100	100 (55.6*)	W m^{-1} K^{-1}
ρ	3120	2400	kg m^{-3}
L	4×10^5		J kg^{-1}
T_e	821.2		K
T_f	921.2		K
κ, κ^A/κ^B	0.3, 0.3/0.15		–
m, m^A/m^B	−340, −340/−720		K
T_W	621.2		K
ΔT	1.0		K
C_0, C_0^A/C_0^B	0.05, 0.025/0.0118		

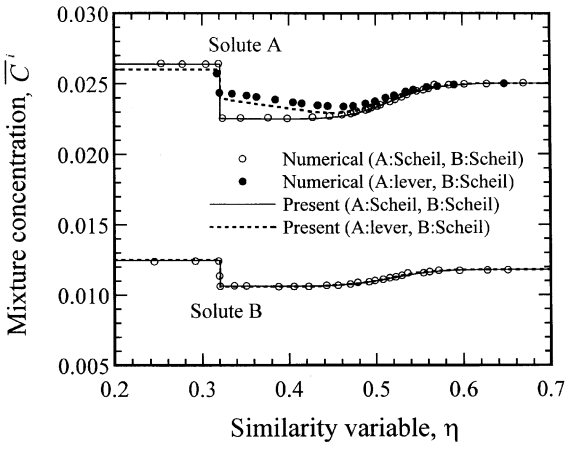

Fig. 3. Comparison of the average concentration profile with the available numerical solution for (i) zero back diffusion for solute A and B and (ii) the complete back diffusion for solute A and zero back diffusion for solute B.

binary system by properly adjusting the phase equilibrium parameters. As $m^{\mathrm{A}}/m_0^{\mathrm{A}}$ increases (i.e., C_0^{A} decreases), the mixture concentration of solute A becomes flatter and approaches zero, and finally goes to a binary system of solute B only.

The mixture concentration $\bar{C}^k$ shown in Figs. 2 and 3, which is the representative parameter to delineate macrosegregation pattern, is defined by the solute conservation for a control volume as

$$\bar{C}^k = \frac{\rho_l(1-f)C_l^k + \rho_s f \bar{C}_s^k}{\rho_l(1-f) + \rho_s f}. \tag{35}$$

The term $\bar{C}_s^k$ in Eq. (35) denotes the intrinsic volume averaged concentration of solute i in the dendritic solid,

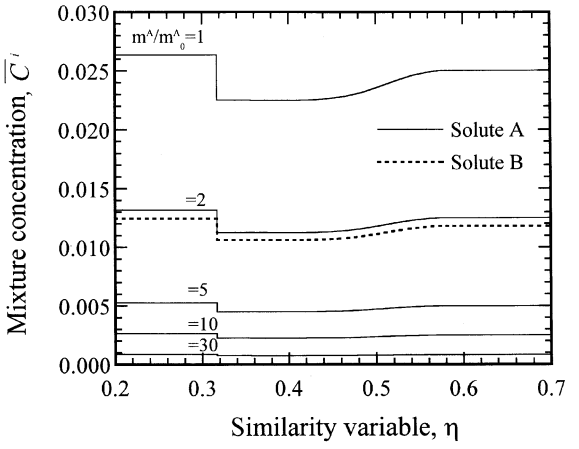

Fig. 4. The asymptotic mixture concentration behavior toward a binary system according to the change of the liquidus slope of solute A.

and can be calculated by solving the following differential equation using Clyne and Kurz model [11]

$$\frac{\mathrm{d}(f\bar{C}_s^k)}{\mathrm{d}\eta} = \kappa^k C_l^k \frac{\mathrm{d}f}{\mathrm{d}\eta} + \beta^k f \kappa^k \frac{\mathrm{d}C_l^k}{\mathrm{d}\eta}. \tag{36}$$

3.2. Features of the present solution

The distinctions between the present and recent works by Voller [11] and Chung et al. [12] are addressed here to highlight the features of present solution. The present solution has common aspects with earlier works [11,12] in that both of them include the shrinkage-induced flow and finite back diffusion, and rely on the same similarity transformation. The present work also follows same features as Chung et al. [12], which include property variation and effective linearized correction scheme for interface position. However, the following features may predominate over the earlier works.

The feasible range of the similarity solution is extended to a ternary or higher-order multicomponent alloy. On the assumption of neglecting inter-diffusion of each solute [6], the transport equations for each solute k have the same form and are independently expressed as Eq. (6). Thus for an alloy of K-solute species, governing equations in the mushy region reduce to $(K+2)$ nonlinear ordinary differential equations via similarity transform, which are to be solved along with the exact solutions for the solid and liquid regions.

Another extension in the present model is to relax the assumption on the partition coefficient defined as $\kappa^k = C_{si}^k/C_l^k$ and microsegregation parameter β^k which are indices of rates of mass diffusion of the elements in the solid phase. Schneider and Beckermann [5] found the direction of flow in the mushy zone was reversed when using the two different data sets which were the same except only for partition coefficients of each solute. They pointed out that partition coefficient has extremely sensitive to the result. This discloses that the assumption invoked by Voller [11] has critical limitations in a practical sense.

Finally, the present solution is also extended to a high degree of the initial superheating by obtaining the exact solution, Eq. (19), in the liquid region. As mentioned earlier, Voller neglected the convection term, and restricted the validity of his solution within a low superheating. He claimed that the convection effect was negligible up to moderate superheating (25 K). However, this deduction should be accepted carefully because the effect may depend strongly on the alloy properties and imposed conditions. The velocity jump across the liquidus caused by this approximation also deviates from the physical reality.

On the whole, the present similarity solution includes the earlier works by Voller [11] and Chung et al. [12] as a

subset, since the present work extends its feasible range over the earlier works without introducing additional assumptions.

3.3. Effects of parameters

The effect of convection in the liquid region on the liquidus position is shown in Fig. 5, for which $\beta = 1$ and numerical data in Table 1 have been used. Even though the liquidus position is the most sensitive physical quantity to the change of superheating, two sets of results with and without convection deviate little from each other. This can be attributed to a low convection-to-conduction ratio for the Al–Cu alloy. The convection effect would be more dominant for an alloy with a small thermal conductivity and large density difference. Nevertheless, the results in Fig. 5 clearly indicate two facts that the progress of the liquidus front is retarded by the inward convection ($\rho_s > \rho_l$), and that the discrepancy increases with enhancing the superheating. Apart from the magnitude of the convection effect, there is no reason to use the approximate solution instead of the exact solution at the same level of compactness.

Fig. 6 demonstrates the effect of variable properties in the mushy region on the solidification behaviors when $\beta = 1$ for the same alloy. The ratios of properties used in the calculation are $\hat{k} = 1.8$ and $\hat{c} = 1.04$ [15], which correspond to the values in parentheses of Table 1. The property differences appear to significantly affect all of the macrosegregation, temperature and solid fraction profiles, while keeping similar trends. These types of quantitative effect favorably support the utility of the present study.

The effects of segregation parameter and partition coefficient are scrutinized for sample ternary alloy (Table 1) and shown in Figs. 7–10, respectively. It should be noted that the present solution can handle a higher-order alloy, but for the purpose of scrutinizing the effect of parameters, we restrict the discussion to a ternary alloy.

As a base condition, we chose 0.15 for the partition coefficients of solute A and B and zero for the segregation parameters of solute A and B. To examine the effect of each parameter, the value of the momentary interest parameter is varied while fixing the rest. Fig. 7 shows the effect of the change in microsegregation parameter of solute A on the average concentration profile of each solute. It is discernible that macrosegregation is reduced as the increase of microsegregation parameter, which is in line with the results of binary alloy [12]. The influence is most remarkable near the solidus in the mushy region where the solid fraction is high enough for $\bar{C}_s^k$ to control

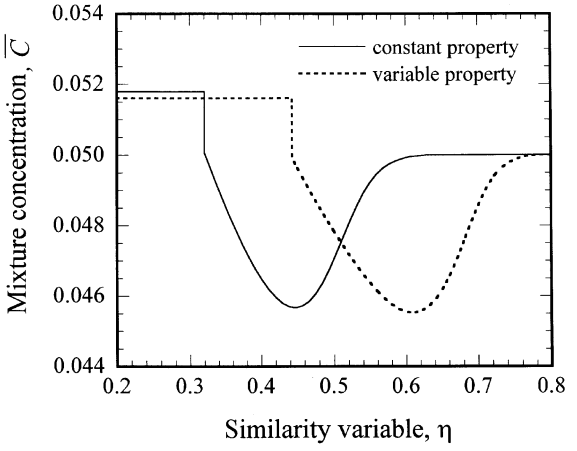

Fig. 6. The effect of variable properties for the lever rule on the average concentration.

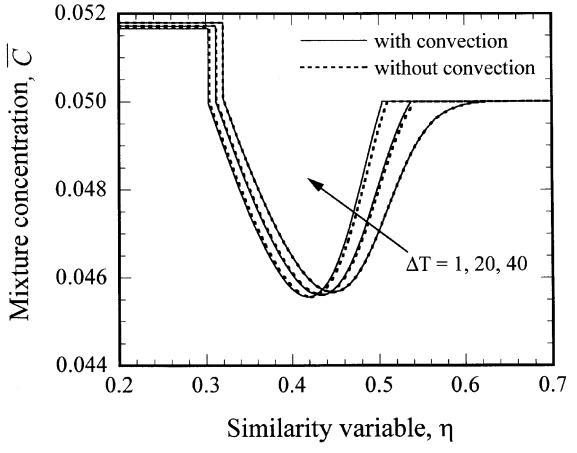

Fig. 5. The effect of convection in the melt on the liquidus position as a function of initial superheating.

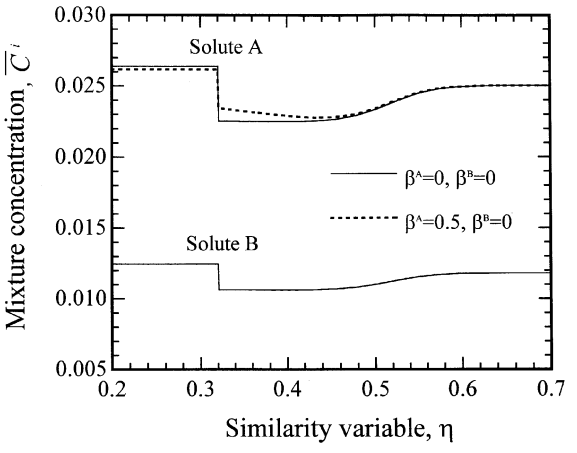

Fig. 7. The effect of the change in microsegregation parameter of solute A on the average concentration profile of each solute.

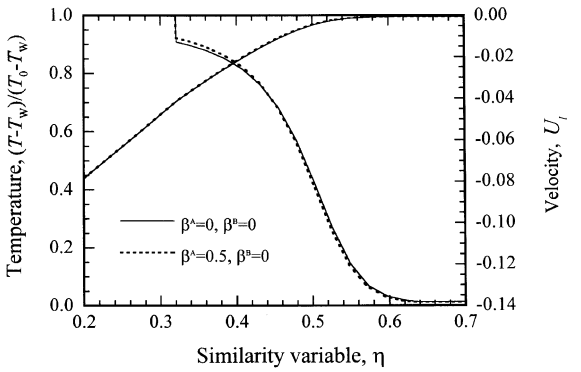

Fig. 8. The effect of the change in microsegregation parameter of solute A on the dimensionless temperature and velocity profiles.

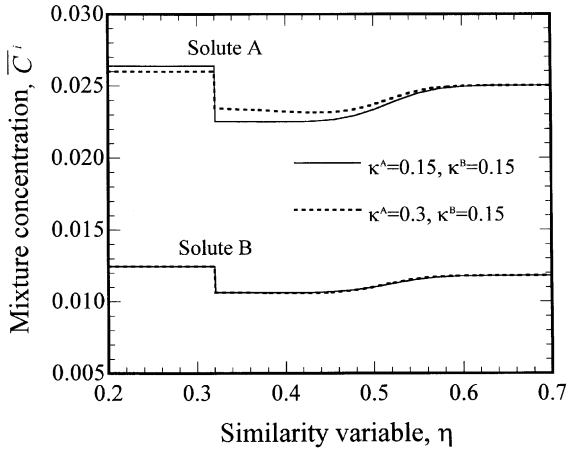

Fig. 9. The effect of the change in partition coefficient of solute A on the average concentration profile of each solute.

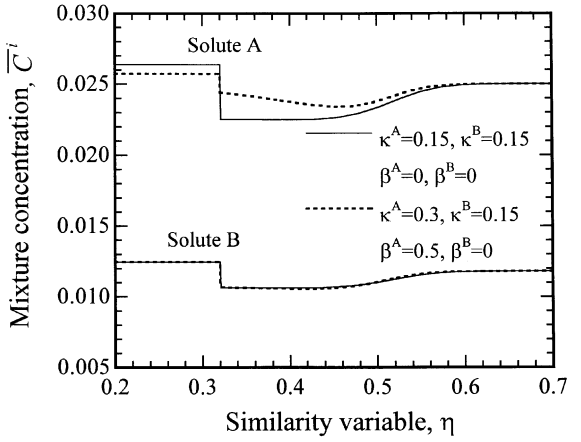

Fig. 10. The combined effect of the changes in both microsegregation and partition coefficient of solute A on the average concentration profile of each solute.

$\bar{C}^k$ in Eq. (35). In contrast, the solidus and liquidus positions remain nearly unchanged despite different values of β^k. This means that microsegregation pertains primarily to the solid fraction field, altering the temperature profile only a little as shown in Fig. 8. The interdendritic flow velocity is related to back diffusion through the solid fraction, as evident in Eq. (20). The more the eutectic is formed with decreasing β^k, the stronger the flow at the solidus.

Fig. 9 shows the effect of the change in partition coefficient of solute A on the average concentration profile of each solute. Large partition coefficient means an increase of inter-dendritic solid concentration [16], which results in the reduction of macrosegregation as shown in Fig. 9. This trend is more pronounced as the effects of β^k and κ^k are combined. Fig. 10 demonstrates the combined effect of these two parameters. The evident reduction of macrosegregation reveals the prominent impacts of β^k and κ^k and the importance of their effects in analysis.

4. Conclusions

Motivated by the limitations involved in the previous analytical approach, the present study has been conducted to establish a more generalized similarity solution for a multicomponent alloy solidification system. Application range of the similarity solution has been extended to a ternary or higher-order multicomponent alloy without any restriction on the microsegregation parameter and partition coefficient which are known to affect macrosegregation significantly. Another extension in the present analysis is capable of handling a high degree of initial superheating by deriving an exact solution in the liquid region with shrinkage-induced flow. For systematically tracking the solidus and liquidus positions, the linearized correction scheme developed for a binary alloy has been adopted in the solution procedure.

The results for representative cases of binary and ternary alloys agree quite well with the existing data, which implies the validity of the present study. In view of the coverage of the model, the present study not only is useful for predicting uni-directional solidification processes, but also serves as a salient test solution for validating sophisticated numerical models.

Acknowledgements

This work was funded by the Brain Korea 21 Project and National CRI Center for Nano Particle Control supported by the Ministry of Science and Technology, Korea.

References

[1] C. Beckermann, R. Viskanta, Mathematical modeling of transport phenomena during alloy solidification, Appl. Mech. Rev. 46 (1993) 1–27.
[2] P.J. Prescott, F.P. Incropera, Convective heat and mass transfer in alloy solidification, Adv. Heat Transfer 28 (1996) 231–238.
[3] J. Ni, F.P. Incropera, Extension of the continuum model for transport phenomena occurring during metal alloy solidification – II. Microscopic considerations, Int. J. Heat Mass Transfer 38 (1995) 1285–1296.
[4] M.C. Schneider, C. Beckermann, A numerical study of the combined effects of microsegregation, mushy zone permeability and flow, caused by volume contraction and thermosolutal convection, on macrosegregation and eutectic formation in binary alloy solidification, Int. J. Heat Mass Transfer 38 (1995) 3455–3473.
[5] M.C. Schneider, C. Beckermann, Formation of macrosegregation by multicomponent thermosolutal convection during the solidification of steel, Metall. and Mater. Trans. A 26 (1995) 2373–2388.
[6] M.J. Krane, F.P. Incropera, D.R. Gaskell, Solidification of ternary metal alloys – I. Model development, Int. J. Heat Mass Transfer 40 (1997) 3827–3835.
[7] M.J. Krane, F.P. Incropera, Solidification of ternary metal alloys – II. Predictions of convective phenomena and solidification behavior in Pb–Sb–Sn alloys, Int. J. Heat Mass Transfer 40 (1997) 3837–3847.
[8] J.C. Muehlbauer, J.D. Hatcher, D.W. Lyons, J.E. Sunderland, Transient heat transfer analysis of alloy solidification, J. Heat Transfer 95 (1973) 324–331.
[9] M.G. Worster, Solidification of an alloy from a cooled boundary, J. Fluid Mech. 167 (1986) 481–501.
[10] S.L. Braga, R. Viskanta, Solidification of a binary alloy solution on a cold isothermal surface, Int. J. Heat Mass Transfer 33 (1990) 745–754.
[11] V.R. Voller, A similarity solution for the solidification of a multicomponent alloy, Int. J. Heat Mass Transfer 40 (1997) 2869–2877.
[12] J.D. Chung, J.S. Lee, S.T. Ro, H. Yoo, An analytical approach to the conduction-dominated solidification of binary mixtures, Int. J. Heat Mass Transfer 42 (1999) 373–377.
[13] C.R. Swaminathan, V.R. Voller, Towards a general numerical scheme for solidification systems, Int. J. Heat Mass Transfer 40 (1997) 2859–2868.
[14] T.W. Clyne, W. Kurz, Solute redistribution during solidification with rapid state diffusion, Metall. Trans. A 12 (1981) 965–971.
[15] B. Basu, J.A. Sekhar, Modeling of multidimensional solidification of an alloy, Metall. Trans. A 20 (1989) 1833–1845.
[16] W. Kurz, D. Fisher, Fundamentals of Solidification, Trans Tech, Aedermannsdorf, Switzerland, 1989.